

Constraining the Chiral Magnetic Effect with charge-dependent azimuthal correlations in Pb-Pb collisions at $\sqrt{s_{NN}} = 2.76$ and 5.02 TeV

Original

Constraining the Chiral Magnetic Effect with charge-dependent azimuthal correlations in Pb-Pb collisions at $\sqrt{s_{NN}} = 2.76$ and 5.02 TeV / Acharya, S.; Adamova, D.; Adolphson, J.; Aggarwal, M.; Rinella, G.; Agnello, M.; Agrawal, N.; Bufalino, S.; Concas, M.; Grosa, F.; Catalano, F.; Fecchio, P.; Balbino, A.. - In: JOURNAL OF HIGH ENERGY PHYSICS. - ISSN 1029-8479. - STAMPA. - 2020:9(2020). [10.1007/JHEP09(2020)160]

Availability:

This version is available at: 11583/2895247 since: 2021-04-18T20:15:58Z

Publisher:

Springer Science and Business Media Deutschland GmbH

Published

DOI:10.1007/JHEP09(2020)160

Terms of use:

This article is made available under terms and conditions as specified in the corresponding bibliographic description in the repository

Publisher copyright

Springer postprint/Author's Accepted Manuscript

This version of the article has been accepted for publication, after peer review (when applicable) and is subject to Springer Nature's AM terms of use, but is not the Version of Record and does not reflect post-acceptance improvements, or any corrections. The Version of Record is available online at: [http://dx.doi.org/10.1007/JHEP09\(2020\)160](http://dx.doi.org/10.1007/JHEP09(2020)160)

(Article begins on next page)

Brick Shaped Antenna Module for Microwave Brain Imaging Systems

D. O. Rodriguez-Duarte, *Student Member, IEEE*, J. A. Tobon Vasquez, *Member, IEEE*,
R. Scapatucci, *Member, IEEE*, L. Crocco, *Senior Member, IEEE* and F. Vipiana, *Senior Member, IEEE*

Abstract—In this letter, we describe and validate a microwave antenna designed for an imaging device for the diagnosis and monitoring of cerebrovascular pathologies. The antenna consists of a printed monopole immersed in a parallelepipedic block of semi-flexible material with custom-permittivity, which allows to avoid the use of liquid coupling media and enables a simple array arrangement. The “brick” is built with a mixture of urethane rubber and graphite powder. The -10 dB frequency band of the antenna is 800 MHz–1.2 GHz, in agreement with the device requirements. The designed brick antenna is assessed in terms of power penetration, reflection and transmission coefficients. To show the performance of the antenna in the relevant application scenario, an experiment has been carried out on an anthropomorphic head phantom, measuring the differential signals between healthy state and hemorrhagic stroke mimicking condition for different antennas positions.

Index Terms—Microwave antennas, microwave imaging, biomedical electromagnetic imaging, brain.

I. INTRODUCTION

Microwave imaging (MWI) is an emerging technology for the diagnosis and follow-up of cerebrovascular pathologies, complementary to current imaging-based technologies, such as magnetic resonance imaging and computed tomography [1], [2]. MWI allows to map the different brain tissues and to distinguish between healthy and unhealthy regions (e.g., ischemic or hemorrhagic stroke zones), based on the contrast of tissues electrical properties at microwave frequencies.

In MWI systems, the antenna array plays a fundamental role, as it has to deliver faithful data to the algorithm in charge of providing the image of the investigated scenario [3]–[8]. This requires a proper design of the radiating element in terms of the choice of a suitable working frequency band, considering that higher frequencies support better spatial resolution, while lower ones reach deeper wave penetration, that impacts on the dynamic range and sensitivity of the receiver. For brain

Manuscript received XXX, 2020; accepted XXX. Date of publication XXX; date of current version XXX. This work was supported by the Italian Ministry of University and Research under the PRIN project “MiBraScan”, and by the European Union’s Horizon 2020 research and innovation program under the EMERALD project, Marie Skłodowska-Curie grant agreement No. 764479. (Corresponding author: Francesca Vipiana)

D. O. Rodriguez-Duarte, J. A. Tobon Vasquez and F. Vipiana are with the Department of Electronics and Telecommunications, Politecnico di Torino, 10129 Torino, Italy (e-mail: francesca.vipiana@polito.it).

R. Scapatucci and L. Crocco are with the Institute for the Electromagnetic Sensing of the Environment, National Research Council of Italy, 80124 Naples, Italy (e-mail: scapatucci.r@irea.cnr.it; crocco.l@irea.cnr.it).

Color versions of one or more of the figures in this letter are available online at <http://ieeexplore.ieee.org>.

Digital Object Identifier XXXXXXXXXXXXXXXXXXXX

imaging, theoretical analysis in [9] experimentally validated in [2, Ch. 2] has shown that a working frequency lower than 1.5 GHz is a convenient choice, due to a “transmission gap” between 1.5 and 4 GHz and the significant decrease of penetration depth occurring at frequencies higher than 4 GHz.

In addition to this, to improve penetration inside the head, a coupling medium is placed between the antenna array and the head surface. Typically, water mixtures with glycerine [4], [8], [10], [11] or Triton X-100 [6], [12] are adopted. However, as the antenna array is immersed in the liquid medium, this solution, while simple, has drawbacks in terms of portability. Moreover, it may introduce limitations in the conformal displacement of the array elements around the head.

The coupling medium is not needed when using (rigid or flexible) on-body antennas, which can improve penetration being attached in almost direct contact with the skin. Different kinds of these antennas have been proposed for biomedical imaging, such as, for instance, planar bowties [13], F-like cavity-backed antennas [14] as well as flexible antennas [15] and arrays [7]. However, if the antenna is attached to head, the tissues in the very near field of the antenna will affect the antenna reflection coefficient, e.g. shifting the designed antenna resonant frequency, in an unpredictable way (due to the patient variability), with possible drawbacks for the imaging algorithm. Moreover, the near-field effects are hard to be modeled and marginally contribute to the reconstruction of the interior imaged domain [16].

In this letter, we describe an antenna which overcomes the above-mentioned issues by exploiting as coupling medium a semi-flexible custom-made material in which the antenna is embedded. As such, we retain the advantages of using a coupling medium (e.g., avoiding near-field effects and making more stable the antenna reflection coefficient), without the need of liquids around the head. Furthermore, thanks to the properties of the adopted material, an easy positioning of the antennas conformal to the head is possible by properly shaping each element as a brick. An example is given in [17] where the proposed antenna, called in the following “brick” antenna, was implemented in a MWI prototype for brain stroke monitoring.

II. BRICK ANTENNA DESIGN AND REALIZATION

According to [9] and [2, Ch. 2], the chosen working frequency band is around 1 GHz, while the coupling medium permittivity is $\epsilon_r \cong 20$; this is a good trade-off between the electromagnetic (EM) penetration inside the head tissues and the spatial imaging resolution. The antenna design takes as

starting point a monopole antenna printed on a slab of standard FR4 (thickness = 1.55 mm, $\epsilon_r = 4.4$ and $\sigma = 0.012$ S/m), which was initially designed to work into a liquid coupling medium [6]. Then, it is optimized to operate in a discrete coupling medium with $\epsilon_r = 20$. The resulted antenna presents a triangular-shaped radiating element, a trimmed back-placed ground plane, and a line, with two stubs designed to improve the antenna matching at the port, fed by a rigid coaxial cable on the back, to add stability and reducing the unwanted variation in the vicinity of the port. Figure 1 shows the optimized prototype, where (a) is the monopole that later is embedded into the brick, as shown in (b). In our design, we adopted an omnidirectional antenna to illuminate the whole region of interest (possibly allowing a reduction of the number of array elements). Moreover, the modification of the near-field antenna pattern due to the antenna operated in the vicinity of an unknown and variable medium (the head) is possibly less pronounced for an omnidirectional antenna.

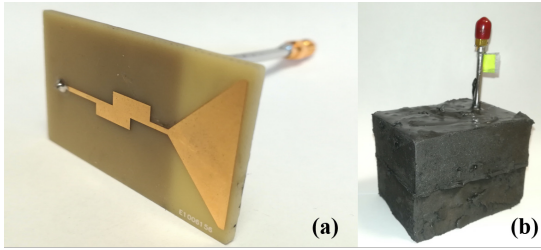


Fig. 1. Brick antenna sample; (a): monopole antenna printed on FR4 substrate; (b): monopole antenna embedded into the brick.

The coupling medium is a discrete brick around the monopole, that keeps a distance of 25 mm between the monopole plane and the brick-head surface in a perfect attaching condition. This distance corresponds to about 0.4 times the wavelength in the coupling medium at 1 GHz, diminishing near-field effects, which are hard to be adequately modeled and only marginally contribute to the image reconstruction [16]. The coupling brick and the radiating part compose together a single unit that is easily included in an array configuration conformal to the head within an MWI system. Moreover, the semi-flexible solid medium gives to the antenna additional mechanical stiffness and stretchiness, improving the robustness of the device and enabling low-degree bends to it, as required to cover the head. In addition, the brick facilitates the portability, and allows different antennas distribution schemes while reducing manufacturing and maintenance costs.

The brick is made of a semi-flexible mixture of urethane rubber and graphite powder (65% and 35% in weight, respectively), whose dielectric characteristics are shown in Fig. 2 (dashed lines). The addition of graphite powder to the rubber is needed to increase the permittivity of the mixture to the designed value (see Fig. 2, lines with dot markers). However, graphite powder increases the conductivity (see Fig. 2, lines with squared markers), but it remains comparable or lower with respect to coupling media used in medical MWI [6], [10].

The final geometrical dimensions of the designed brick antenna are listed in Table I (refer to Fig. 3 for the geometrical meaning labels). The area of the front (radiating part of the

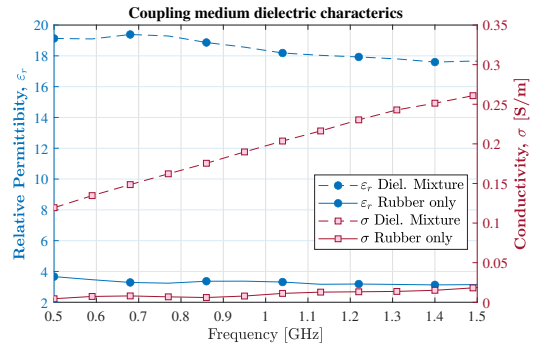


Fig. 2. Coupling medium dielectric characteristics versus frequency

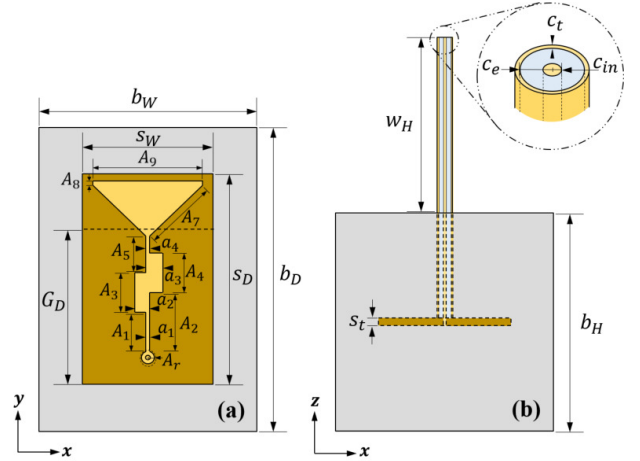


Fig. 3. Antenna geometry; (a): top-view on the antenna plane; (b): side-view on the antenna port.

proposed brick antenna is equal to 5×7 cm² (see Table I): considering that the average area of the upper part of a human head is about 1000 cm², it is possible to place up to 28 brick antennas around it, which is slightly larger than the number of antennas identified by the design procedure in [18], [19].

TABLE I
DIMENSIONS (MM) OF THE BRICK ANTENNA (SEE FIG. 3)

Label	Value	Label	Value	Label	Value	Label	Value
A_1	9.09	A_7	1.00	a_4	1.00	b_W	50.00
A_2	13.59	A_8	25.28	G_D	35.40	b_H	50.00
A_3	9.00	A_r	1.50	s_W	30.00	w_H	40.00
A_4	9.00	a_1	1.00	s_D	48.00	c_t	0.29
A_5	8.50	a_2	2.44	s_t	1.55	c_e	1.51
A_6	16.72	a_3	2.90	b_D	70.00	c_{in}	0.47

III. NUMERICAL AND EXPERIMENTAL RESULTS

Here, we analyze the performance of the brick antenna. All simulations are performed with the WIPL-D Pro software, that is a full-wave solver based on method-of-moments with high-order basis functions [20]. In the experiments, the antenna scattering parameters have been measured with the vector network analyzer (VNA) Keysight N5227A [21].

For the numerical simulations, the human head is modeled employing a computer-aided design (CAD) of a standard

anthropomorphic adult head, considering two cases: the first one, “UH”, is a uniform head phantom consisting of a single medium having the average properties among head tissues. The second, “MTH”, is a multiple-tissues phantom mimicking the complex structure of the head as shown in Fig. 4.(a). Table II reports the dielectric properties of each tissue at 1 GHz, where “CSF” refers to the cerebrospinal fluid and “Avg.” to the head-average tissue. For the experimental validations, a single cavity 3-D anthropomorphic head phantom is used. The phantom has been realized by additive manufacturing with a 3-D plastic printer and filled up with a liquid mixture made of Triton X-100, water and salt, that has the same dielectric characteristics of the head-average tissue used in simulations [22].

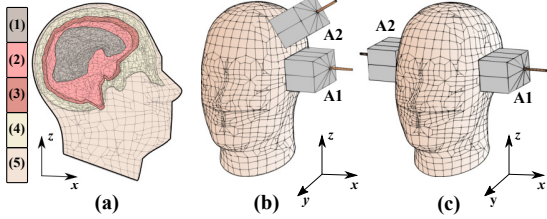


Fig. 4. CAD head phantom and brick antennas' configurations; (a): cross-section view of the MTH model; (b): close antenna pair configuration (LLS); (c) left-to-right-side antenna pair configuration (LRS).

TABLE II

TISSUES' DIELECTRIC PROPERTIES FOR HEAD MODELS (SEE FIG. 4).

1 GHz	Gray matter	White matter	CSF	Bone	Avg.
Label	(1)	(2)	(3)	(4)	(5)
ϵ_r	52.28	38.58	68.44	12.36	45.38
σ (S/m)	0.985	0.622	2.455	0.156	0.77

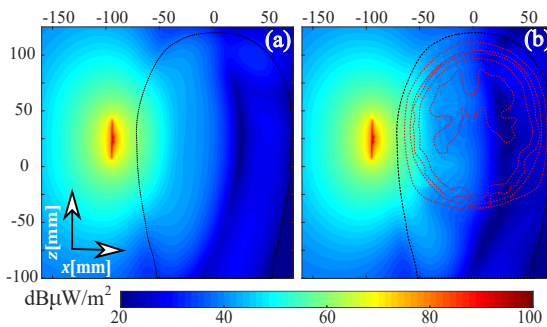


Fig. 5. Power density distribution at 1 GHz placing the monopole antenna immersed in the coupling medium infinitely extended around the head, coronal view; (a): UH model; (b) MTH model.

The first analyses consider the EM wave penetration into the head and the impact of introducing a small air-gap between the brick antenna and the head surface. Taking as best-case scenario the one where the monopole antenna is immersed in the coupling medium infinitely extended around the head, the corresponding power density distribution is computed with both head models and shown in Fig. 5. Since the best-case scenario reveals a good penetration, the subsequent analysis examines the case of the proposed brick antenna close to the head (with air all around) and varying the air-gap between the brick and the head surface from 0 mm (where the brick

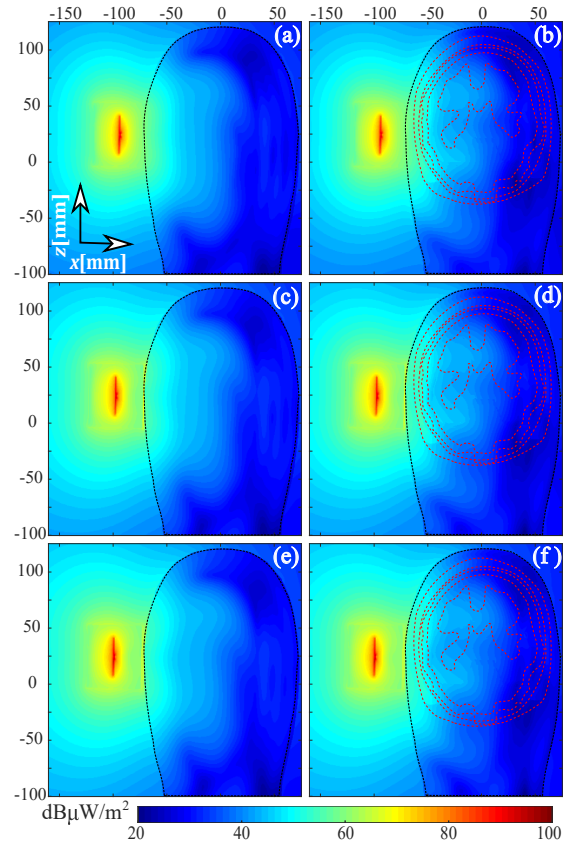


Fig. 6. Power density distribution at 1 GHz placing the brick antenna at different air-gap distances from the head surface, coronal view; left column: UH model, right column: MTH model; (a)-(b): no gap; (c)-(d): 1 mm gap; (e)-(f): 3 mm gap

adheres perfectly to the head surface) to 3 mm, as shown in Fig. 6. As it can be seen, with both head models, limiting the coupling medium just around the monopole antenna (i.e., using the brick antenna) as well as the possible presence of air-gaps between the brick antenna and the head surface have a limited effect on the power density distribution within the head with respect to the best-case scenario.

The antenna reflection coefficient, S_{11} , has been then assessed varying the air-gap between the brick and the head surface. Fig. 7.(a) reports the simulated $|S_{11}|$ for the two considered head models: the brick antenna matched perfectly at 1 GHz, showing slight bandwidth variation as the head model and/or the air-gap change. The measured $|S_{11}|$ is shown in Fig. 7.(b) where two realized brick antennas are considered (labelled as “A1” and “A2”). The measurements behave in agreement with the simulations, manifesting just a down-shift of the resonant frequency of about 50 MHz, possibly due to manufacturing inaccuracies. The measured -10 dB bandwidth is from 800 MHz to 1.2 GHz covering the desired working frequency range [9], [2, Ch. 2].

To assess the capability of the antenna to provide meaningful data for MWI, the transmission of the signal through the head has been evaluated. In particular, the transmission coefficient, S_{12} , has been assessed for a close antenna pair configuration, labelled as “LLS”, and a left-to-right-side one, labelled as “LRS”, see Figs. 4.(b)-(c). Figure 8 compares the

simulated and measured $|S_{12}|$ for a 3 mm air-gap with the UH model, chosen to have the same conditions in simulations and measurements. The highlighted bands represent the range of values for a set of around ten simulations/measurements varying slightly the position and/or the orientation of the brick antennas, while the inner lines are the corresponding average values. The simulated and measured $|S_{12}|$ are comparable to each other for both antenna configurations, though the measured LRS one (i.e., with opposite antennas) is less smooth, possibly due to external interferences. Moreover, in all cases, the $|S_{12}|$ is well above the VNA noise floor [21]. Finally, Table III compares the realized brick antenna with respect to other antennas used in brain MWI devices, showing that its transmission performance are in line with the literature.

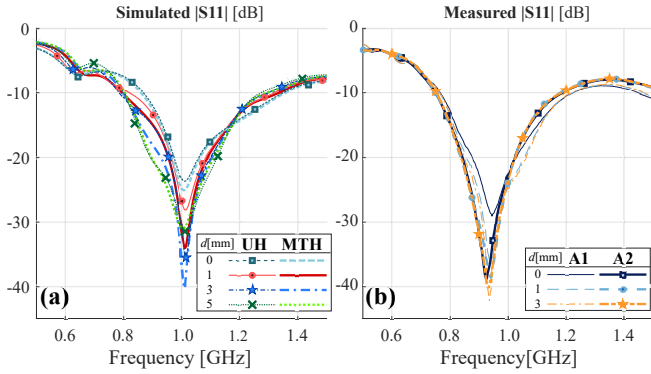


Fig. 7. Reflection coefficient amplitude for different air-gaps between the brick and the head surface, d [mm]. (a): simulations, considering the two head models (b): measurements, considering two realized antennas.

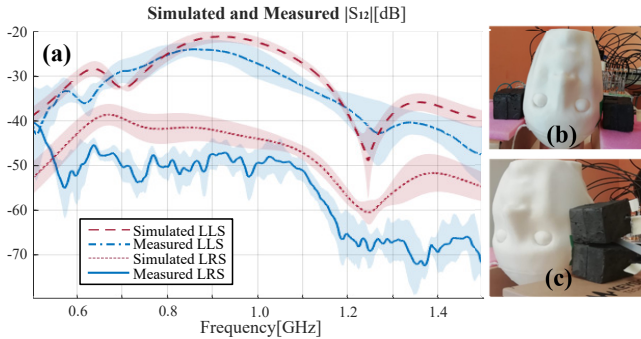


Fig. 8. (a): Simulated and measured transmission coefficient amplitudes, $|S_{12}|$, for the LLS and LRS configurations; (b)-(c): experimental setup for the LRS and LLS configurations, respectively.

TABLE III
ANTENNA PERFORMANCE COMPARISON WITH PREVIOUS PUBLICATIONS

Ref.	-10 dB freq. band [GHz]	Dimensions [mm]	Kind	Medium	$ S_{12} $ [dB] LLS / LRS
Here	0.8 – 1.2	$50 \times 50 \times 70^\dagger$	omni.	solid	-26 / -50
[6]	0.8 – 2.0	$30 \times 38 \times 1.7$	omni.	liquid	NA / -51
[7]*	1.0 – 1.4	$60 \times 85 \times 4$	dir.	on-body	-15 / NA
[15]	1.0 – 2.5	$25 \times 28 \times 5.6$	dir.	on-body	-28 / NA
[23]	1.2 – 1.5	$40 \times 46 \times 14.4$	dir.	on-body	-20 / -40
[24]	0.8 – 2.5	$29 \times 18 \times 2$	omni.	liquid	-30 / -55

† the antenna dimensions include the coupling medium, i.e. the brick

*the reported data are for the antenna labelled as “1” in [7]

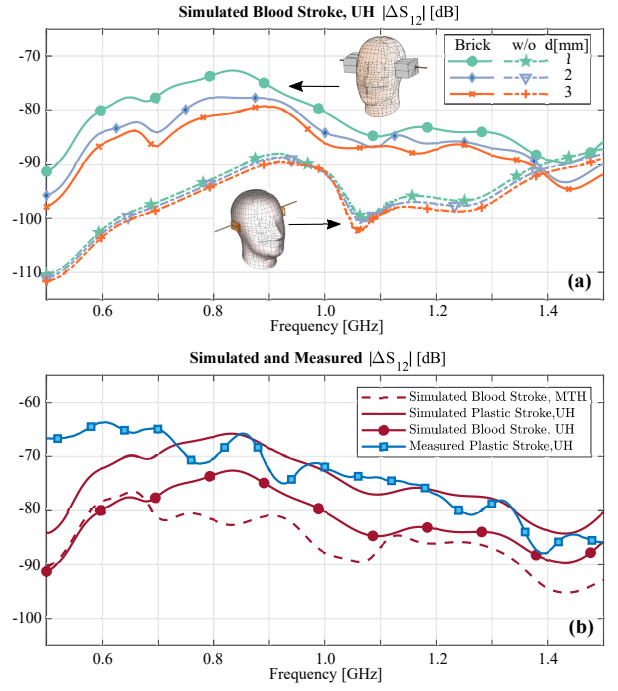


Fig. 9. Differential transmission coefficients, LRS configuration; (a): simulated blood stroke using an antenna pair with and without the dielectric bricks; (b): simulated and measured plastic/blood stroke with a pair of brick antennas.

To consider the antenna capabilities in the actual operational environment, a 12.5 mm-radius sphere, mimicking a stroke, is introduced in the phantom for the LRS configuration (i.e., the worst-case scenario). To show the effect of the stroke, the differential transmission coefficient, ΔS_{12} , computed as the difference between the S_{12} values with and without the sphere, has been appraised in Fig. 9. In simulations, the sphere was filled either with blood ($\epsilon_r = 61$ and $\sigma = 1.6$ S/m at 1 GHz) and with lossless plastic ($\epsilon_r = 2.3$), which is the case considered in the experiment. In the case of a blood sphere and for different air-gaps, Fig. 9.(a) shows that the simulated $|\Delta S_{12}|$ using a pair of brick antennas are higher than using the same antennas but without the bricks, demonstrating so a better field penetration if the brick is present. In Fig. 9.(b), a good agreement between simulations and measurements (plastic sphere) can be observed. In the simulated case of a blood sphere, ΔS_{12} is around 10 dB lower in all the frequency range, also using the MTH model, but still within the VNA dynamic [21].

IV. CONCLUSION AND PERSPECTIVES

A modular brick antenna for microwave brain imaging has been proposed. The brick is made of a semi-flexible dielectric coupling medium around a monopole printed antenna. The brick antenna is well-matched between 0.8 and 1.2 GHz, with strong robustness under different setup variations. It has an adequate EM wave penetration inside the head, and it is able to discriminate the presence of a spherical stroke area with a radius of 12.5 mm. The observed results suggest that the proposed brick antenna is suitable for microwave brain imaging devices, as initially shown in [17].

ACKNOWLEDGMENT

The authors would like to acknowledge the valuable support of Prof. Branko Kolundzija and WIPL-D team, providing WIPL-D Pro software in the frame of the MSCA EMERALD project. Moreover, the 3-D anthropomorphic head phantom was provided by Prof. Nadine Joachimowicz and Prof. Bernard Duchêne in the frame of the PRIN MIBRASCAN project.

REFERENCES

- [1] K. B. Walsh, "Non-invasive sensor technology for prehospital stroke diagnosis: Current status and future directions," *Int. J. Stroke*, vol. 14, pp. 592–602, Jul. 2019.
- [2] L. Crocco, I. Karanasiou, M. James, and R. C. Conceicao (Eds.), *Emerging Electromagnetic Technologies for Brain Diseases Diagnostics, Monitoring and Therapy*. Springer int. pub., 2018.
- [3] A. T. Mobashsher and A. M. Abbosh, "On-site rapid diagnosis of intracranial hematoma using portable multi-slice microwave imaging system," *Scientific Reports*, vol. 6, pp. 1–17, Nov. 2016.
- [4] M. Hopfer, R. Planas, A. Hamidipour, T. Henriksson, and S. Semenov, "Electromagnetic tomography for detection, differentiation, and monitoring of brain stroke: A virtual data and human head phantom study," *IEEE Antennas Propag. Mag.*, vol. 59, pp. 86–97, Oct. 2017.
- [5] A. Fhager, S. Candefjord, M. Elam, and M. Persson, "Microwave diagnostics ahead: Saving time and the lives of trauma and stroke patients," *IEEE Microwave Mag.*, vol. 19, pp. 78–90, May 2018.
- [6] J. A. Tobon Vasquez, R. Scapatucci, G. Turvani, G. Bellizzi, N. Joachimowicz, B. Duchêne, E. Tedeschi, M. R. Casu, L. Crocco, and F. Vipiana, "Design and experimental assessment of a 2D microwave imaging system for brain stroke monitoring," *Int. J. Antennas Propag.*, no. Article ID 8065036, p. 12 pages, 2019.
- [7] A. S. M. Alqadami, K. S. Bialkowski, A. T. Mobashsher, and A. M. Abbosh, "Wearable electromagnetic head imaging system using flexible wideband antenna array based on polymer technology for brain stroke diagnosis," *IEEE Trans. Biomed. Circuits Syst.*, vol. 13, pp. 124–134, Feb. 2019.
- [8] O. Karadima, M. Rahman, J. Sotiriou, N. Ghavami, P. Lu, S. Ahsan, and P. Kosmas, "Experimental validation of microwave tomography with the DBIM-TwIST algorithm for brain stroke detection and classification," *SENSORS*, vol. 20, Feb. 2020.
- [9] R. Scapatucci, L. D. Donato, I. Catapano, and L. Crocco, "A feasibility study on Microwave Imaging for brain stroke monitoring," *Prog. Electromagn. Res. B*, vol. 40, pp. 305–324, 2012.
- [10] P. M. Meaney, F. Shubitidze, M. W. Fanning, M. Kmiec, N. R. Epstein, and K. D. Paulsen, "Surface wave multipath signals in near-field microwave imaging," *International Journal of Antennas and Propagation*, vol. 2012, no. Article ID 697253, p. 11 pages, 2012.
- [11] E. Razzicchia, I. Sotiriou, H. Cano Garcia, E. Kallos, G. Palikaras, and P. Kosmas, "Feasibility study of enhancing microwave brain imaging using metamaterials," *SENSORS*, vol. 19, 12 2019.
- [12] M. R. Casu, M. Vacca, J. A. Tobon Vasquez, A. Pulimeno, I. Sarwar, R. Solimene, and F. Vipiana, "A COTS-based microwave imaging system for breast-cancer detection," *IEEE Trans. Biomed. Circuits Syst.*, vol. 11, pp. 804–814, Aug. 2017.
- [13] X. Li, M. Jalilvand, Y. L. Sit, and T. Zwick, "A compact double-layer on-body matched bowtie antenna for medical diagnosis," *IEEE Transactions on Antennas and Propagation*, vol. 62, pp. 1808–1816, April 2014.
- [14] M. Rokunuzzaman, A. Ahmed, T. C. Baum, and W. S. T. Rowe, "Compact 3-D antenna for medical diagnosis of the human head," *IEEE Transactions on Antennas and Propagation*, vol. 67, pp. 5093–5103, Aug 2019.
- [15] A. S. M. Alqadami, N. Nguyen-Trong, B. Mohammed, A. E. Stancombe, M. T. Heitzmann, and A. Abbosh, "Compact unidirectional conformal antenna based on flexible high-permittivity custom-made substrate for wearable wideband electromagnetic head imaging system," *IEEE Transactions on Antennas and Propagation*, vol. 68, pp. 183–194, Jan 2020.
- [16] O. M. Bucci, L. Crocco, and T. Isernia, "Improving the reconstruction capabilities in inverse scattering problems by exploitation of close-proximity setups," *J. Opt. Soc. Am. A*, vol. 16, pp. 1788–1798, Jul. 1999.
- [17] J. A. Tobon Vasquez, R. Scapatucci, G. Turvani, G. Bellizzi, D. O. Rodriguez-Duarte, N. Joachimowicz, B. Duchene, E. Tedeschi, M. R. Casu, L. Crocco, and F. Vipiana, "A prototype microwave system for 3D brain stroke imaging," *SENSORS*, May 2020.
- [18] R. Scapatucci, J. Tobon, G. Bellizzi, F. Vipiana, and L. Crocco, "Design and numerical characterization of a low-complexity microwave device for brain stroke monitoring," *IEEE Transactions on Antennas and Propagation*, vol. 66, no. 12, pp. 7328–7338, 2018.
- [19] O. M. Bucci, L. Crocco, R. Scapatucci, and G. Bellizzi, "On the design of phased arrays for medical applications," *Proc. IEEE*, vol. 104, pp. 633–648, Mar. 2016.
- [20] WIPL-D d.o.o., "WIPL-D PRO description." Accessed on: Feb. 28, 2020. [Online]. Available: <https://wipl-d.com/products/wipl-d-pro/>.
- [21] Keysight Technologies, "Keysight 2-port and 4-port PNA network analyzer, N5227A 10 MHz to 67 GHz," *Data Sheet and Technical Specifications*, Apr. 2019.
- [22] N. Joachimowicz, B. Duchêne, C. Conessa, and O. Meyer, "Anthropomorphic breast and head phantoms for microwave imaging," *Diagnostics*, vol. 85, pp. 1–12, Dec. 2018.
- [23] M. Persson, A. Fhager, H. D. Trefnà, Y. Yu, T. McKelvey, G. Pegegnius, J. E. Karlsson, and M. Elam, "Microwave-based stroke diagnosis making global prehospital thrombolytic treatment possible," *IEEE Trans. Biomed. Eng.*, vol. 61, pp. 2806–2817, Nov. 2014.
- [24] N. Ghavami, I. Sotiriou, and P. Kosmas, "Preliminary experimental validation of radar imaging for stroke detection with phantoms," in *2019 Photonics Electromagnetics Research Symposium - Fall (PIERS - Fall)*, pp. 1916–1923, 2019.